Incommensurate antiferromagnetic order in the manifoldly-frustrated SrTb2O4 with transition temperature up to 4.28 K

Hai-Feng Li, Cong Zhang, Anatoliy Senyshyn, Andrew Wildes, Karin Schmalzl, Wolfgang Schmidt, Martin Boehm, E. Ressouche, Binyang Hou, Paul Meuffels, et al.

frontiers in PHYSICS

ORIGINAL RESEARCH ARTICLE
published: 21 July 2014
doi: 10.3389/fphy.2014.00042

Incommensurate antiferromagnetic order in the manifoldly-frustrated $SrTb_2O_4$ with transition temperature up to 4.28 K

Hai-Feng Li[1,2]*, Cong Zhang[2], Anatoliy Senyshyn[3], Andrew Wildes[4], Karin Schmalzl[1], Wolfgang Schmidt[1], Martin Boehm[4], Eric Ressouche[5], Binyang Hou[6], Paul Meuffels[7], Georg Roth[2] and Thomas Brückel[8]*

[1] Jülich Centre for Neutron Science JCNS, Forschungszentrum Jülich GmbH, Outstation at Institut Laue-Langevin, Grenoble, France
[2] Institut für Kristallographie der RWTH Aachen University, Aachen, Germany
[3] Forschungsneutronenquelle Heinz Maier-Leibnitz FRM-II, Technische Universität München, Garching bei München, Germany
[4] Institut Laue-Langevin, Grenoble, France
[5] SPSMS, UMR-E 9001, CEA-INAC/UJF-Grenoble 1, MDN, Grenoble, France
[6] European Synchrotron Radiation Facility, Grenoble, France
[7] Peter Grünberg Institut PGI and JARA-FIT, Forschungszentrum Jülich GmbH, Jülich, Germany
[8] Jülich Centre for Neutron Science JCNS and Peter Grünberg Institut PGI, JARA-FIT, Forschungszentrum Jülich GmbH, Jülich, Germany

Edited by:
Olga Kazakova, National Physical Laboratory, UK

Reviewed by:
Sean Langridge, Science and Technology Facilities Council, UK
Irina Yakimenko, Linköping University, Sweden
Jasper Altman Drisko, University of Maryland, College Park, USA

***Correspondence:**
Hai-Feng Li, Jülich Centre for Neutron Science JCNS, Forschungszentrum Jülich GmbH, Outstation at Institut Laue-Langevin, 71 Avenue des Martyrs, BP 156, F-38042 Grenoble Cedex 9, France; Institut für Kristallographie der RWTH Aachen University, Jaegerstrasse 17-19, D-52056 Aachen, Germany
e-mail: hfli@ill.fr;
Thomas Brückel, Jülich Centre for Neutron Science JCNS and Peter Grünberg Institut PGI, JARA-FIT, Forschungszentrum Jülich GmbH, Leo-Brandt-Straße, D-52425 Jülich, Germany
e-mail: t.brueckel@fz-juelich.de

The Néel temperature of the new frustrated family of $SrRE_2O_4$ (RE = rare earth) compounds is yet limited to ∼0.9 K, which more or less hampers a complete understanding of the relevant magnetic frustrations and spin interactions and an exploration of potential interesting properties. Here we report on a new frustrated member to the family, $SrTb_2O_4$ with a record $T_N = 4.28(2)$ K, and an experimental study of the magnetic interacting and frustrating mechanisms by polarized and unpolarized neutron scattering. The compound $SrTb_2O_4$ displays an incommensurate antiferromagnetic (AFM) order with a transverse wave vector $\mathbf{Q}_{\mathrm{AFM}}^{0.5\mathrm{K}} = (0.5924(1), 0.0059(1), 0)$ albeit with partially-ordered moments, 1.92(6) μ_B at 0.5 K, stemming from only one of the two inequivalent Tb sites mainly by virtue of their different octahedral distortions. The localized moments are confined to the *bc* plane, 11.9(66)° away from the *b* axis probably by single-ion anisotropy. We reveal that this AFM order is dominated mainly by dipole-dipole interactions and disclose that the octahedral distortion, nearest-neighbour (NN) ferromagnetic (FM) arrangement, different next NN FM and AFM configurations, and in-plane anisotropic spin correlations are vital to the magnetic structure and associated multiple frustrations. The discovery of the thus far highest AFM transition temperature renders $SrTb_2O_4$ a new friendly frustrated platform in the family for studying the nature of magnetic interactions and frustrations and exploring potential macroscopic functionalities and new quantum states.

Keywords: new frustrated compound, highest transition temperature, single crystal, antiferromagnetism, octahedral distortion, single-ion anisotropy

1. INTRODUCTION

Revealing the magnetic coupling mechanism is often a critical step toward understanding the role of magnetism in intriguing phenomena such as colossal magnetoresistance (CMR), high T_C superconductivity, multiferroicity or frustration in correlated electron materials [1–5]. By way of example, the indirect double- and super-exchange interactions were successfully elaborated in qualitatively explaining the CMR effect and associated magnetic orders based only on the spin and charge degrees of freedom [1]. In 4*f*-based insulators, the indirect oscillating interaction [4–7] between pairs of localized 4*f* moments via the intermediary of valence electrons is blocked. Therefore, possible super-, dipole-dipole and multipolar, and Dzyaloshinsky-Moriya (DM) exchange interactions are primarily responsible for potential magnetic ordering [4]. Without detailed knowledge of the structural and magnetic parameters, it is hard to uniquely determine which interaction acts as the major exchange mechanism [8]. In this case, the origins of the related incommensurable spin structures become elusive [4]. In addition, the competition between spin-orbital coupling and crystal electric field (CEF) at low temperatures largely affects the highly-degenerate Hund's rule ground state, and besides the anisotropic dipolar and DM interactions, determine the magnitude of the magnetic anisotropy [9, 10]. This anisotropy strongly influences the degree of magnetic

frustration. Sometimes, it may disorder or even quench potential magnetic moments, leading to a virtually nonmagnetic ground state [11].

Magnetic frustration can lead to novel quantum states such as spin liquid, spin ice, cooperative paramagnetism or the magnetic Coulomb phase based on magnetic monopole excitations, providing an excellent testing ground for theories [4, 12–25]. A Monte Carlo simulation indicates that the observed diffuse scattering in $SrEr_2O_4$ originates from a ladder of Er triangles [26]. A computation of the crystal-field levels demonstrates site-dependent anisotropic single-ion magnetism in the compounds of $SrHo_2O_4$ and $SrDy_2O_4$ [27]. Lanthanide-based magnetic compounds, e.g., edge-sharing tetrahedra, corner-sharing spinels, or triangular Kagomé and pyrochlore lattices, often show anomalous magnetic properties due to geometric frustration [28–31]. The family of $SrRE_2O_4$ (RE = Y, Gd, Ho, Yb) compounds was first synthesized in 1967 [32]. Recently, a study on polycrystalline $SrRE_2O_4$ (RE = Gd, Dy, Ho, Er, Tm, Yb) samples demonstrates that they adopt the orthorhombic structure [33] with a geometric frustration for the magnetic ions revealed by the existence of magnetic short-range orders down to ∼1.5 K [34]. Subsequently, single crystals of $SrRE_2O_4$ (RE = Y, Lu, Dy, Ho, Er) were successfully grown [35]. Single-crystal neutron-scattering studies on $SrRE_2O_4$ (RE = Ho, Er, Yb) compounds

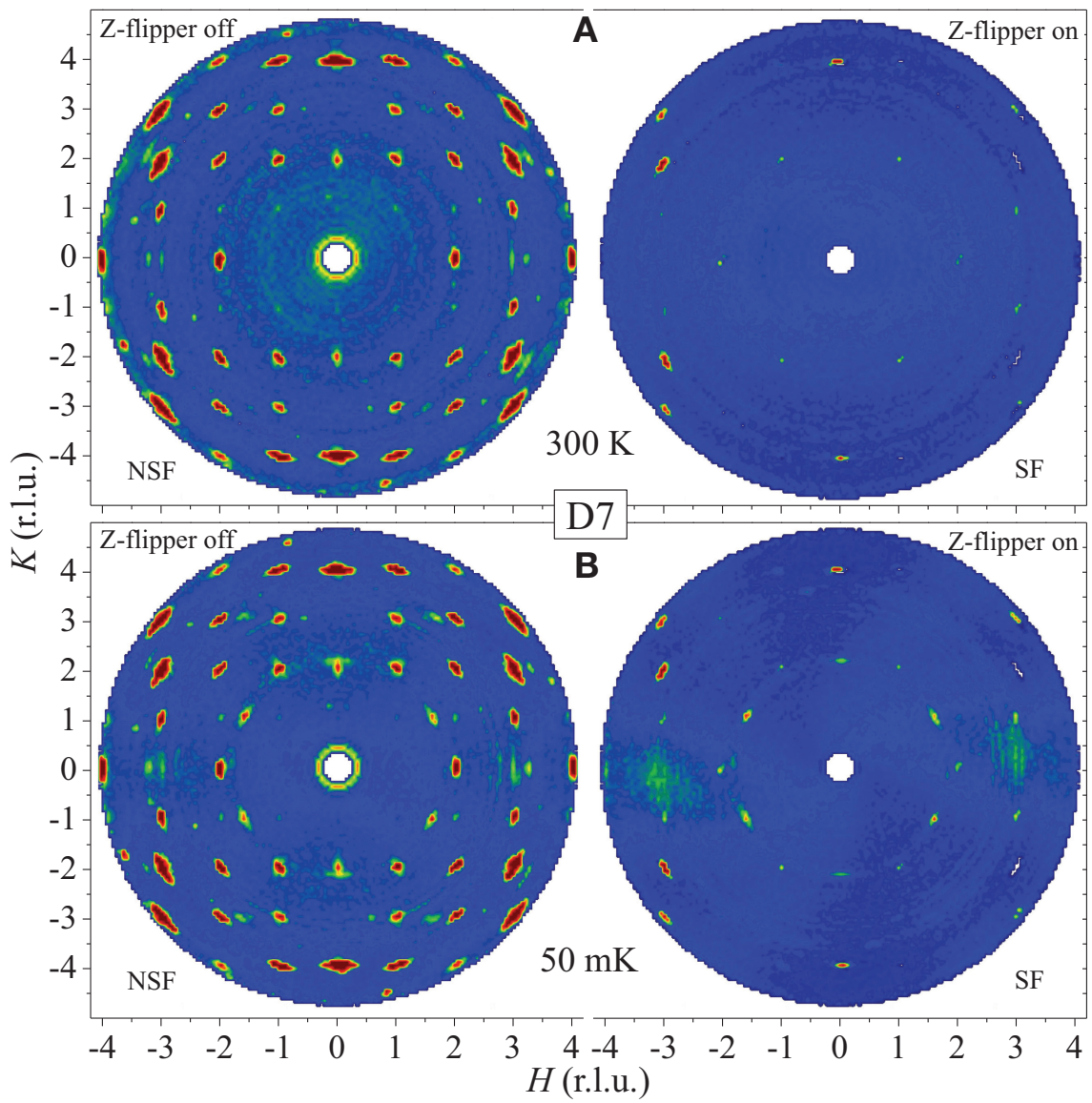

FIGURE 1 | Polarization analysis data measured using D7 (ILL). (A) At 300 K. **(B)** At 50 mK. The NSF (i.e., Z-flipper off, left panel) and SF (i.e., Z-flipper on, right panel) channels are shown with the same color code for intensity. The non-perfect polarization involuntarily leads to the presence of some nuclear Bragg peaks, e.g., (0, ±4, 0), in the SF channel at both temperatures. The horizontal bar-shaped neutron-scattering intensities around (0, ±2.15, 0) and the extremely-broad diffuse scattering around (±3, 0, 0) in **(B)** may correspond to some short-range magnetic components. It is pointed out that similar diffuse magnetic scattering also appears in the $SrHo_2O_4$ and $SrEr_2O_4$ single crystals [36–38].

with respective antiferromagnetic (AFM) transition temperatures at 0.62, 0.73, and 0.9 K were reported [36–40], generally confirming that there exists a coexistence of long- and short-range magnetic orders. It is pointed out that for the case of $SrHo_2O_4$, Young et al. [41] observed only a short-range spin order inconsistent with other reports [36, 37, 40]. Further experimental tests would be necessary to address this discrepancy. Since the adopted orthorhombic structure accommodates two *RE* sites (*RE1* and *RE2*), it is hard to derive the crystallographic origins of the two types of spin ordering. In addition, single-crystal $SrDy_2O_4$ displays only weak diffuse magnetic scattering which persists down to ∼20 mK [42]. The low transition temperatures of the magnetic orders, to some extent, prevent a complete understanding of the nature of magnetic interactions and frustrations in the family. To overcome these problems and address the relevant interesting physics necessitate a search in the $SrRE_2O_4$ (*RE* = rare earth) family for a new compound that displays a higher Néel temperature, thus permitting a technically easier study of the two coupling mechanisms.

In this study, we report on a new frustrated member to the family of $SrRE_2O_4$, namely $SrTb_2O_4$, which has not been studied yet by neutron scattering. The single-crystal $SrTb_2O_4$ displays a long-range magnetic order relative to the underlying lattice. The noncollinear incommensurate AFM structure forms at $T_N = 4.28(2)$ K upon cooling. The synthesis of $SrTb_2O_4$ with the highest Néel temperature in the family opens up an easier route to elucidate the magnetic coupling and frustrating mechanisms. By polarized and unpolarized neutron scattering we uniquely determine the detailed structural and magnetic parameters to understand the magnetism in $SrTb_2O_4$.

2. MATERIALS AND METHODS

Polycrystalline samples of $SrTb_2O_4$ were synthesized from stoichiometric mixtures of $SrCO_3$ (99.99%) and Tb_4O_7 (99.99%) compounds by standard solid-state reaction [43]. Both raw materials were preheated at 800° for 12 h and weighted at ∼200°. The mixed and milled raw materials were calcined twice at 1473 and 1573 K for 48 h each in air in order to perform decarbonization and prereaction. The resulting powder was pressed into cylindrical rods with an isostatical pressure of ∼78 MPa. The rods were sintered two times at 1573 and 1673 K for 48 h at each temperature in air. After each round of the isostatic pressing and subsequent firing, the product was reground and ball-remilled, which results in a dense and homogenous sample and ensures a complete chemical reaction. The single crystal of $SrTb_2O_4$ was grown by optical floating-zone method with an atmosphere of ∼98% Ar and ∼2% O_2. The growing speed is ∼4 mm/h with rotations of the feed and seed rods at +32 and −28 rpm, respectively. The phase purity of the polycrystalline and single-crystalline samples was checked by in-house X-ray powder diffraction. The electrical resistivity of a bar-shaped single crystal by standard dc four-probe technique was measured on a commercial physical property measurement system.

High-resolution neutron powder diffraction (NPD) patterns were collected with a pulverized $SrTb_2O_4$ single crystal (∼5 g) mounted in a ^{3}He insert on the structure powder diffractometer (SPODI) [44] with constant wavelength λ = 2.54008(2) Å at the FRM-II research reactor in Garching, Germany.

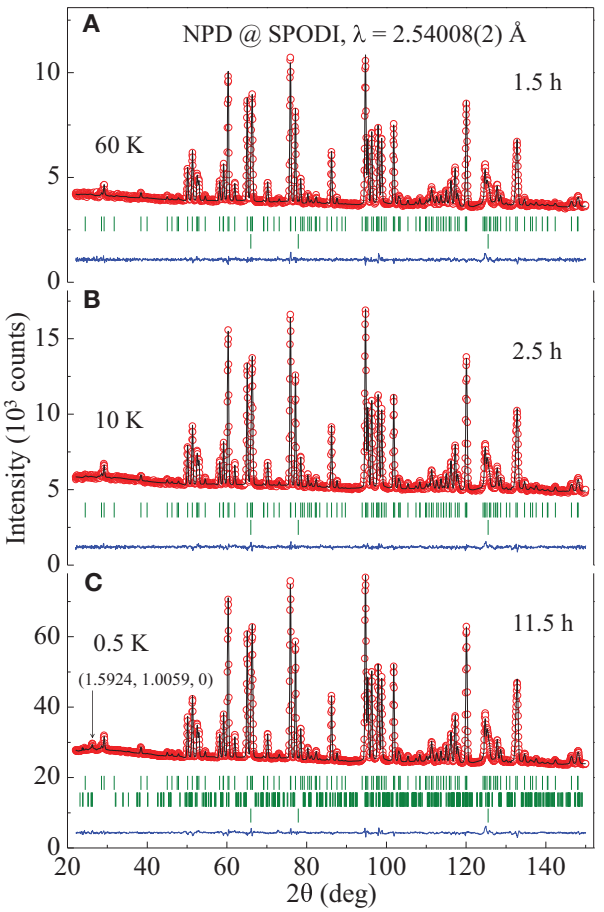

FIGURE 2 | Observed (circles) and calculated (solid lines) NPD patterns from the study using SPODI (FRM-II). (A) At 60 K with counting time ∼1.5 h. **(B)** At 10 K with counting time ∼2.5 h. **(C)** At 0.5 K with counting time ∼11.5 h. The vertical bars mark the positions of nuclear and magnetic Bragg reflections of $SrTb_2O_4$ as well as the Al nuclear Bragg peaks (from sample environment), respectively. The lower curves represent the difference between observed and calculated patterns. No obvious diffuse magnetic scattering appears as observed in polycrystalline $SrRE_2O_4$ (*RE* = Ho, Er, Dy) compounds in Ref. [34].

The $SrTb_2O_4$ single crystal (∼2.2 g) for the neutron-scattering studies was oriented in the (*H*, *K*, 0) scattering plane with the neutron Laue diffractometer OrientExpress [45] and the IN3 thermal triple-axis spectrometer at the Institut Laue-Langevin (ILL), Grenoble, France. The mosaic of this single crystal is 0.494(5)° full width at half maximum (FWHM) for the nuclear (2, 0, 0) Bragg reflection at 1.5 K. Longitudinal *XYZ* neutron polarization analysis [46] was carried out on the D7 (ILL) diffractometer with a dilution fridge and λ = 4.8 Å. Unpolarized elastic neutron-scattering studies were performed at the two-axis D23 diffractometer (ILL) with incident wavelength 1.277 Å and the IN12 (ILL) cold triple-axis spectrometer with fixed final energy

of 5.3 meV and the beam collimation set as open-40′-sample-60′-open.

Here the wave vector $\mathbf{Q}_{(HKL)}$ (Å^{-1}) $= (\mathbf{Q}_H, \mathbf{Q}_K, \mathbf{Q}_L)$ is defined through $(H, K, L) = (\frac{a}{2\pi}Q_H, \frac{b}{2\pi}Q_K, \frac{c}{2\pi}Q_L)$ quoted in units of r.l.u., where a, b, and c are relevant lattice constants referring to the orthorhombic [33] unit cell.

3. RESULTS

Figure 1 shows the neutron polarization analysis in the spin-flip (SF, i.e., Z-flipper on) and non-spin-flip (NSF, i.e., Z-flipper off) channels. Compared with the maps at 300 K (**Figure 1A**), it is clear that extra fourfold Bragg peaks around $(\pm 1.6, \pm 1, 0)$ appear symmetrically in both SF and NSF reciprocal space maps at 50 mK (**Figure 1B**) due to a long-range magnetic transition. Polarized neutron magnetic scattering depends on the direction of the neutron polarization $\hat{\mathbf{P}}$ with respect to the scattering vector $\hat{\mathbf{Q}}$, and also the direction of the ordered-moments $\hat{\mu}$. In our case, $\hat{\mathbf{P}}$ (Z-component) $\parallel$ c-axis [46], and the magnetic Bragg reflections are observed in the $(H, K, 0)$ plane, i.e., $\hat{\mathbf{P}} \perp \hat{\mathbf{Q}}$. In this case, the neutron-scattering cross sections of the NSF and SF channels are

$$\left(\frac{d\sigma}{d\Omega}\right)^{\mathrm{NSF}}_{\mathrm{Z\text{-}off}} = \frac{1}{2}\left(\frac{d\sigma}{d\Omega}\right)_{\mathrm{mag}} + \frac{1}{3}\left(\frac{d\sigma}{d\Omega}\right)_{\mathrm{si}} + \left(\frac{d\sigma}{d\Omega}\right)_{\mathrm{nuc}},$$
$$\left(\frac{d\sigma}{d\Omega}\right)^{\mathrm{NSF}}_{\mathrm{mag}} \propto \langle \hat{\mu} \parallel \hat{\mathbf{P}} \rangle^2, \text{ and} \quad (1)$$

$$\left(\frac{d\sigma}{d\Omega}\right)^{\mathrm{SF}}_{\mathrm{Z\text{-}on}} = \frac{1}{2}\left(\frac{d\sigma}{d\Omega}\right)_{\mathrm{mag}} + \frac{2}{3}\left(\frac{d\sigma}{d\Omega}\right)_{\mathrm{si}},$$
$$\left(\frac{d\sigma}{d\Omega}\right)^{\mathrm{SF}}_{\mathrm{mag}} \propto \langle \hat{\mu} \perp \hat{\mathbf{P}} \times \hat{\mathbf{Q}} \rangle^2, \quad (2)$$

respectively. The first and the second terms in each equation refer to the magnetic and spin-incoherent scatterings, respectively. The third term in Eq. (1) denotes nuclear and isotope incoherent contributions [46]. The presence of the incommensurable AFM Bragg peaks in the NSF channel (**Figure 1B**) indicates that one

Table 1 | Refined structural parameters (lattice constants, atomic positions, Debye-Waller factor *B*, bond angles and bond lengths), magnetic moment $\hat{\mu}$, and the corresponding goodness of refinement by the Fullprof Suite [47] from the NPD data measured at 0.5, 10, and 60 K using SPODI (FRM-II).

Pulverized $SrTb_2O_4$ single crystal (Orthorhombic, space group *Pnam*, $Z = 4$)									
T (K)	0.5			10			60		
a, b, c (Å)	10.0842 (1)	11.9920 (2)	3.4523 (1)	10.0844 (1)	11.9918 (1)	3.4522 (1)	10.0852 (1)	11.9922 (1)	3.4525 (1)
Atom	x	y	B (Å^2)	x	y	B (Å^2)	x	y	B (Å^2)
Sr	0.7497 (1)	0.6487 (1)	0.85 (5)	0.7493 (2)	0.6485 (2)	0.87 (7)	0.7498 (3)	0.6491 (3)	1.04 (8)
Tb1	0.4243 (2)	0.1126 (1)	0.27 (4)	0.4241 (2)	0.1124 (2)	0.25 (5)	0.4250 (3)	0.1123 (2)	0.56 (6)
Tb2	0.4182 (2)	0.6116 (1)	0.47 (4)	0.4180 (2)	0.6116 (2)	0.50 (5)	0.4178 (3)	0.6114 (2)	0.53 (7)
O1	0.2133 (2)	0.1799 (1)	0.64 (5)	0.2138 (3)	0.1798 (2)	0.75 (7)	0.2125 (3)	0.1796 (2)	0.63 (9)
O2	0.1293 (2)	0.4818 (1)	0.16 (5)	0.1295 (2)	0.4819 (2)	0.21 (7)	0.1288 (3)	0.4824 (2)	0.43 (9)
O3	0.5092 (2)	0.7859 (2)	0.56 (4)	0.5095 (2)	0.7857 (2)	0.48 (6)	0.5095 (3)	0.7859 (3)	0.69 (8)
O4	0.4273 (2)	0.4216 (1)	0.55 (5)	0.4271 (3)	0.4218 (2)	0.49 (7)	0.4270 (4)	0.4217 (2)	0.74 (9)
$\hat{\mu}$(Tb1) (μ_B)	b-axis: +1.88 (8), c-axis: +0.40 (23)								
∠Tb1-O2-Tb1 (°)	92.3 (1), 96.7 (1)			92.4 (1), 96.6 (1)			92.6 (1), 96.7 (2)		
∠Tb1-O3-Tb1 (°)	102.3 (1)			102.2 (1)			102.4 (1)		
∠Tb1-O1-Tb2 (°)	114.1 (1)			114.1 (2)			114.0 (2)		
∠Tb1-O3-Tb2 (°)	128.7 (1)			128.8 (2)			128.7 (2)		
∠Tb2-O1-Tb2 (°)	95.8 (1)			95.8 (1)			96.2 (1)		
∠Tb2-O4-Tb2 (°)	94.1 (1), 101.3 (1)			93.9 (1), 101.3 (1)			93.8 (1), 101.2 (2)		
∠O1-Tb1-O2 (°)	172.1 (2), 91.2 (1)			172.3 (2), 91.3 (1)			171.7 (2), 91.0 (2)		
∠O2-Tb1-O3 (°)	171.8 (1), 89.9 (1)			172.0 (1), 89.9 (1)			172.2 (2), 90.3 (2)		
∠O3-Tb2-O4 (°)	154.0 (1), 83.7 (1)			153.9 (2), 83.6 (1)			153.8 (3), 83.5 (2)		
∠O1-Tb2-O4 (°)	168.3 (1), 112.0 (1)			168.3 (2), 112.0 (2)			168.0 (2), 112.1 (2)		
⟨Tb1-O1,2,3⟩ (Å)	2.3088 (8)			2.3084 (10)			2.3073 (13)		
⟨Tb2-O1,3,4⟩ (Å)	2.3220 (8)			2.3232 (11)			2.3216 (14)		
Δ ($\times 10^{-4}$)	Tb1: 10.905, Tb2: 1.894			Tb1: 10.729, Tb2: 2.077			Tb1: 9.987, Tb2: 2.079		
R_p, R_{wp}, R_{exp}, χ^2	1.73, 2.28, 1.46, 2.44			2.38, 3.06, 3.08, 0.986			2.83, 3.65, 3.95, 0.856		

The calculated average bond-lengths ⟨Tb1-O1,2,3⟩ and ⟨Tb2-O1,3,4⟩ and the extracted octahedral distortion parameter Δ are also listed. All atoms reside in the Wyckoff site 4c, i.e., (x, y, 0.25). Number in parenthesis is the estimated standard deviation of the last significant digit.

component of $\hat{\mu}$ is parallel to the *c* axis, while their appearances in the SF channel imply a $\hat{\mu}$ component lying in the *ab* plane.

We observe the magnetic Bragg peak only at 0.5 K in our NPD study (**Figure 2**). We thereby refine the AFM wave vector exactly as $\mathbf{Q}_{\mathrm{AFM}} = (0.5924(1), 0.0059(1), 0)$ by the profile-matching mode [47] and a total moment $|\hat{\mu}| = 1.92(6)\mu_{\mathrm{B}}$ at the maximum amplitude for the Tb1 ions only with the *b*- and *c*-components equalling to $+1.88(8)$ and $+0.40(23)$ μ_{B} (**Table 1**), respectively. The moment size of the Tb2 site is negligible. **Figure 3** schematically shows the resulting crystal and magnetic structures as well as the structural parameters for the bent Tb_6 honeycombs. The temperature dependence of the AFM (1.6, 1, 0) Bragg peak is shown in **Figure 4**. The extracted integrated intensity (I) was fit to a power law $I = I_0(1 - \frac{T}{T_{\mathrm{N}}})^{\beta}$, which produces a Néel temperature $T_{\mathrm{N}} = 4.28(2)$ K, and a critical exponent $\beta = 0.55(2)$ probably indicative of a second-order type phase transition and possible three-dimensional Heisenberg-like spin interactions [48].

We record a reciprocal space map (**Figure 5A**) around the AFM (1.6, 1, 0) Bragg peak at 1.7 K using D23, and the central scans along the q_H and q_K directions (**Figure 5B**) were measured at IN12. In both figures, the FWHM of the magnetic Bragg peak along the q_H and q_K directions is sharply different. Both magnetic Bragg peaks are broader than the nuclear Bragg (2, 0, 0) reflection in the reciprocal space as shown in **Figure 5B**, which indicates that the observed magnetic Bragg peaks are beyond the

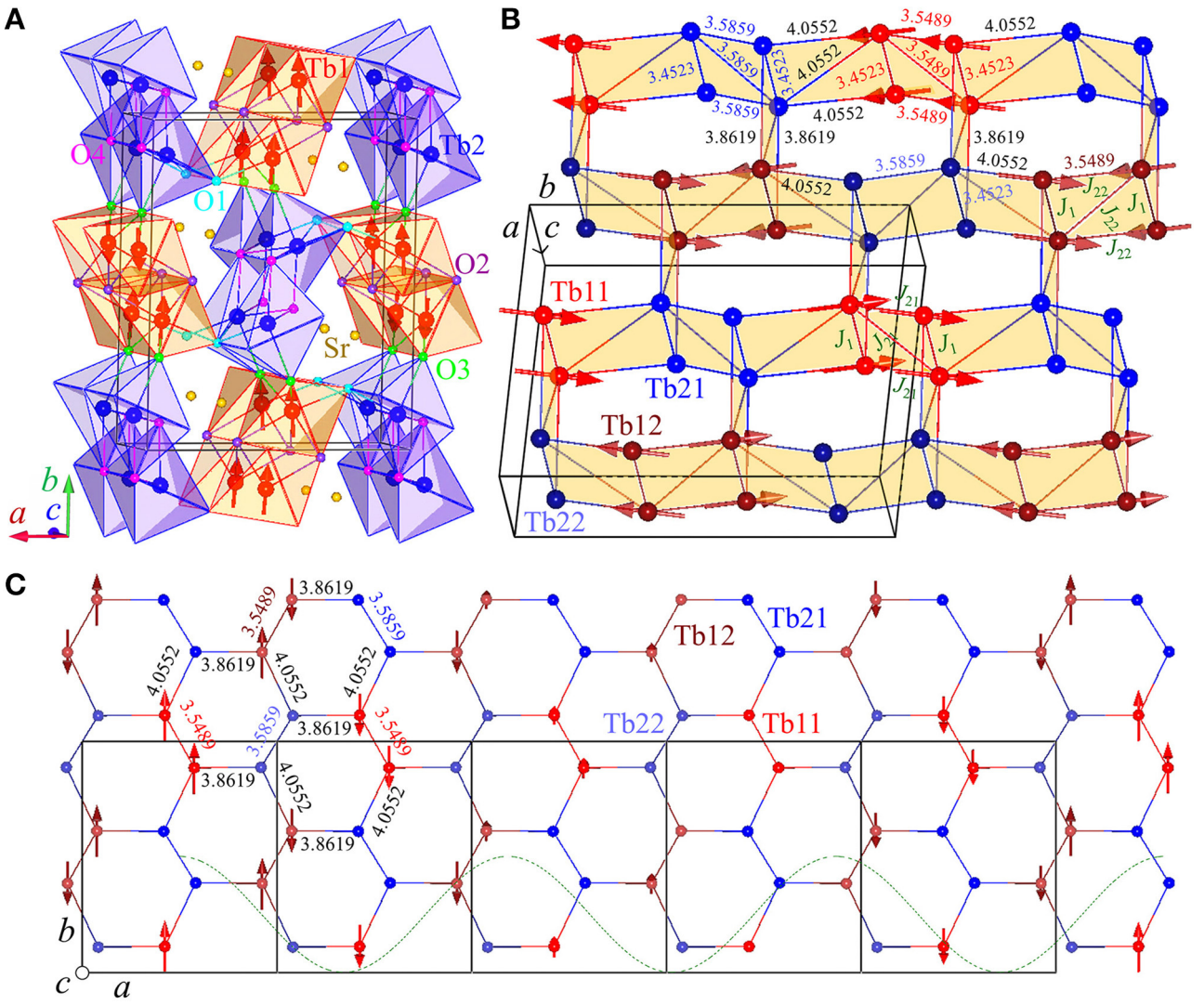

FIGURE 3 | Crystal and magnetic structures of $SrTb_2O_4$. (A) As refined with the SPODI (FRM-II) data measured at 0.5 K. **(B)** Detailed Tb-Tb bond lengths within the bent Tb_6 honeycombs. J_1 and J_{21}/J_{22} represent the nearest-neighbor (NN) and next-NN (NNN) magnetic couplings. **(C)** Projection of the bent Tb_6 honeycombs to the *ab* plane. The cosine-curve (dashed line) beginning from the center of the first unit-cell in left schematically shows the incommensurable spin modulation along the *a* axis. In **(A–C)**, the arrows drawn through the Tb1 ions represent the Tb1 partially-ordered moments, and the connected lines represent the crystallographic unit cell(s). To clearly show the magnetic frustration, Tb1 and Tb2 sites in **(A)** are transferred into Tb11 and Tb12 as well as Tb21 and Tb22 sites, respectively, as shown in **(B,C)** by the irreducible representation analysis to the *P*-1 symmetry [47].

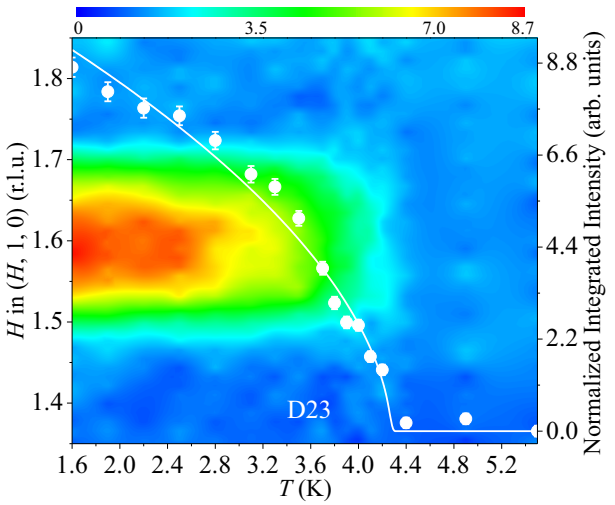

FIGURE 4 | Temperature-dependent ordering parameter of the AFM transition. Temperature dependent *H*-scans around the AFM (1.6, 1, 0) Bragg peak (left ordinate) performed at D23 (ILL) and the corresponding integrated intensities (circles) (right ordinate). The solid line is the fit with a power law as described in the text. The error bars are statistical errors.

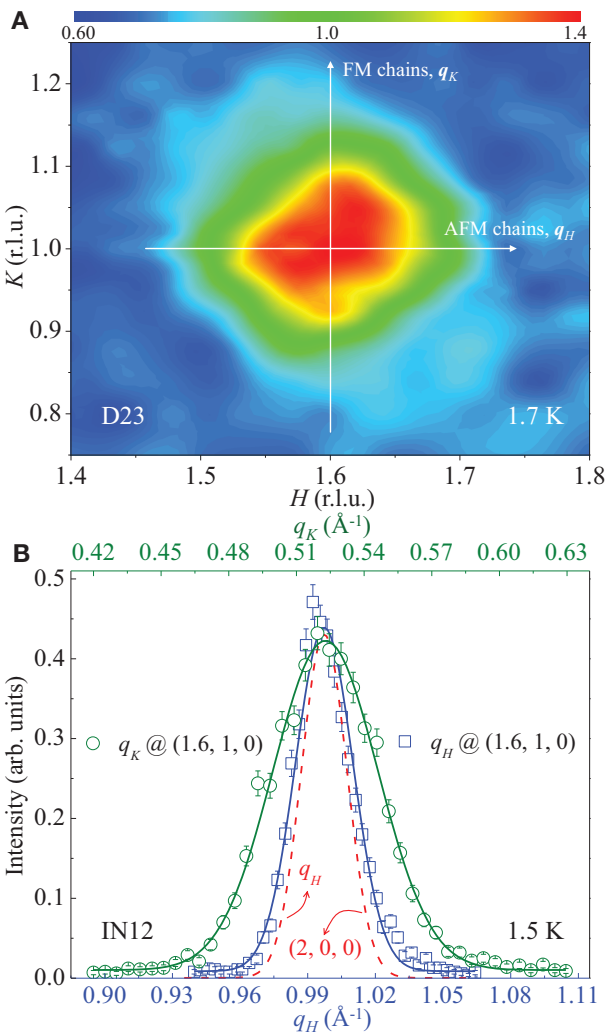

FIGURE 5 | Anisotropic in-plane spin correlations of $SrTb_2O_4$. (A) Unpolarized neutron data around the AFM (1.6, 1, 0) Bragg reflection measured at 1.7 K using D23 (ILL). The two perpendicular arrows point out the directions of $\boldsymbol{q}_H$ (i.e., the in-plane AFM chains) and $\boldsymbol{q}_K$ (i.e., the in-plane FM chains), respectively. **(B)** Unpolarized neutron data around the (1.6, 1, 0) (void symbols) and the (2, 0, 0) (dashed line) Bragg peaks measured at 1.5 K using IN12 (ILL). For comparison, the q_H values around the nuclear (2, 0, 0) Bragg peak are reduced by 0.2547 Å^{-1}. The solid lines are Gaussian fits to the magnetic data convoluted with the nuclear correlation length as expected **Q**-resolution.

instrument resolution. Therefore, **Figure 5B** shows a real in-plane magnetic anisotropy.

4. DISCUSSION

To quantitatively estimate the in-plane anisotropy, we take the FWHM of the nuclear Bragg (2, 0, 0) peak as the detecting accuracy which is convoluted in fitting the magnetic peaks by a Gaussian function shown as the solid lines in **Figure 5B**. This results in FWHM = 0.0183(1) and 0.0492(2) Å^{-1} along the q_H and q_K directions, respectively, implying highly anisotropic in-plane spin correlations consistent with the observation that strong magnetic frustration exists in $SrTb_2O_4$. We roughly estimate the spin-correlation length (ξ) by $\xi = \frac{2\pi}{\mathrm{FWHM}}$, i.e., $\xi_H = 343.7(22)$ Å and $\xi_K = 127.6(4)$ Å. Therefore, $\frac{\xi_H}{\xi_K} = 2.69(2)$. Similar in-plane anisotropic magnetic correlations were also observed in the iron-based superconductors [49–53] that are highly frustrated, too, where its microscopic origin, from the ellipticity of the electron pockets or the competing exchange interactions associated with the local-moment picture, is still highly debated [54–57]. It is undoubted that the observed in-plane magnetic anisotropy in $SrTb_2O_4$ indicates an appearance of the competing spin exchanges and is certainly associated with a description of the purely-localized magnetism of ionic Tb^{3+} ions. A deeper understanding of the insulating state necessitates theoretical band structure calculations. We tentatively estimate the compatibility between ordered magnetic and nuclear crystalline domains based on the non-deconvoluted FWHM (κ) of the Bragg (1.6, 1, 0) ($\kappa_m = 0.0300(7)$ Å^{-1}) and (2, 0, 0) ($\kappa_n = 0.0238(2)$ Å^{-1}) peaks, i.e., $\kappa_n/\kappa_m = 79(2)\%$, which implies that the incommensurate AFM structure orders in a long-range fashion relative to the underlying lattice of the single crystal.

We further analyze the spin-correlation length with our NPD data (**Figure 2C**). Firstly, it is pointed out that the positive and negative momenta cannot technically be differentiated in a NPD study. As shown in **Figure 6A**, taking into account the corresponding SPODI instrument resolution (dashed line) [46], a Gaussian fit (solid line) to the AFM Bragg (1.5924, 1.0059, 0) peak (squares) results in an average $\xi_{\mathrm{AFM}} = 864(36)$ Å in real space. This indicates that the AFM ordering observed in $SrTb_2O_4$ is indeed of long range in character in comparison with the reported extremely-broad magnetic diffuse scattering which was attributed to the presence of short-ranged magnetic ordering in polycrystalline $SrRE_2O_4$ (RE = Ho, Er, Dy) samples in the study of Ref. [34]. With the same method utilized in **Figure 6A**,

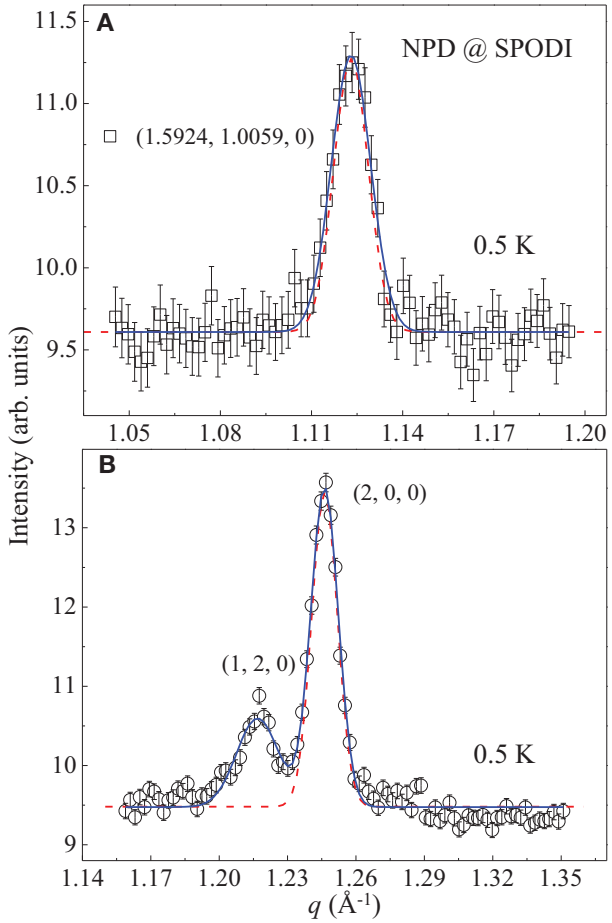

FIGURE 6 | NPD peaks of the incommensurate AFM (1.5924, 1.0059, 0) and the nuclear Bragg (2, 0, 0) reflections. The data were measured at 0.5 K using SPODI (FRM-II) and extracted from **Figure 2C**. **(A)** NPD data of the incommensurate AFM (1.5924, 1.0059, 0) Bragg reflection (squares), and **(B)** of the nuclear Bragg (1, 2, 0) and (2, 0, 0) reflections (circles). The solid lines are Gaussian fits convoluted with the corresponding Q-resolutions (dashed lines) [46].

we also analyze the NPD peak of the nuclear Bragg (2, 0, 0) reflection as shown in **Figure 6B** and extract that $\xi_{(200)} = 1304(34)$ Å. This indicates that $\xi_{AFM}/\xi_{(200)} = 66(3)\%$ basically in accord with the compatibility between ordered magnetic and nuclear crystalline domains extracted with our single-crystal neutron-scattering data. Since our NPD data were collected from a pulverized $SrTb_2O_4$ single crystal, that ξ_{AFM} is ~2.5 times larger than ξ_H may indicate that there have strong magnetic and crystalline domain effects in single-crystal $SrTb_2O_4$, or a large part of spins are blocked probably due to a pining effect by strains accumulated during single crystal growth. In any case, this difference between single-crystalline and polycrystalline samples in turn supports the fact that there is a strong magnetic frustration in single-crystal $SrTb_2O_4$. Further studies with high pressures would be of great interest.

In most cases, the strength of the indirect magnetic interactions such as conventional double- or super-exchange [1] can be influenced more or less by the value of the revelent bond angle [58–61], e.g., the ∠Tb-O-Tb bond angles in $SrTb_2O_4$ as listed in **Table 1** (see also **Figure 7**). However, the respective values of ∠Tb-O-Tb display no appreciable difference within accuracy between 0.5 and 10 K (**Table 1**), below and above the T_N, respectively, which may indicate an invalidity of the two conventional magnetic coupling mechanisms (double- or super-exchange) in $SrTb_2O_4$. This is consistent with the study of $SrTm_2O_4$ [11] and in excellent agreement with our transport study, where any attempts to measure possible resistivity in $SrTb_2O_4$ from 2 to 300 K were fruitless. We estimate that the resistance of the single crystal measured is beyond at least 10^6 ohm. We thus conclude that $SrTb_2O_4$ is a robust insulator, and the electrons responsible for the incommensurable antiferromagnetism are mainly from the localized $4f^8$ shell of the ionic Tb^{3+} ions. In this localized picture, the interionic exchange interactions dominate for the formation of the magnetic structure [4, 6]. The nearest Tb neighbors are stacked linearly along the *c* axis (**Figure 3B**). The shortest Tb1-Tb1 and Tb2-Tb2 have the same bond length. However, the NN Tb1 ions have a ferromagnetic (FM) arrangement. By contrast, the interaction between the NN Tb2 ions is blocked unexpectedly (**Figure 3B**). There is no appreciable difference in the NN Tb-Tb bond length, i.e., the *c* lattice constant, between 0.5 and 10 K (**Table 1**), which probably rules out the potential direct exchange interaction consistent with the fact that unpaired 4*f* electrons are deeply embedded under the $5s^2p^6$ shells and also indicates that the prevalent dipole-dipole interaction is subjected to some condition, i.e., the octahedral distortion as discussed below, in agreement with the study of $SrTm_2O_4$ [11].

As a non-Kramers ion, Tb^{3+} ($S = 3, L = 3, J = 6, g_J = 1.5$) in principle keeps the time reversal symmetry and doesn't show any energy degeneracy in the presence of the purely-localized electric field. However, we refine two kinds of octahedra as shown in **Figure 7**: $Tb1O_6$ and $Tb2O_6$, corresponding to the partially-ordered and totally-frozen Tb1 and Tb2 ions, respectively. The average octahedral distortion [58, 59] can be quantitatively measured by the parameter Δ defined as: $\Delta = \frac{1}{6}\sum_{n=1}^{6}\left[\frac{(d_n-\langle d\rangle)}{\langle d\rangle}\right]^2$, where d_n and $\langle d\rangle$ are the six Tb-O bond lengths along the six crossed directions (**Figure 7**) and the mean Tb-O bond length (**Table 1**), respectively. It is noteworthy that the Δ values of the Tb1 and Tb2 ions are in the same magnitudes as those of the Mn^{3+} Kramers and Mn^{4+} non-Kramers ions, respectively, in the Jahn-Teller (JT) distorted regime of single-crystal $La_{\frac{7}{8}}Sr_{\frac{1}{8}}MnO_3$ [60]. This sharp contrast implies that the Tb1 ions are strongly distorted, while the Tb2 ions behave normally within the non-Kramers scheme. Therefore, the Δ magnitude that reflects the ion local symmetry and thus the strength of the surrounding CEF directly determines the existence of the magnetic ordering, which is supported by the observation that below T_N the respective Δ values of the Tb1 and Tb2 ions change oppositely with temperature (**Figure 8**). We therefore infer that one possible reason for the formation of the incommensurable magnetic structure is the modulated distribution of the $4f^16s^2$ valence electrons which modify the surrounding environment experienced by the localized unpaired 4*f* electrons. The corresponding modulation of the local symmetry may plausibly be

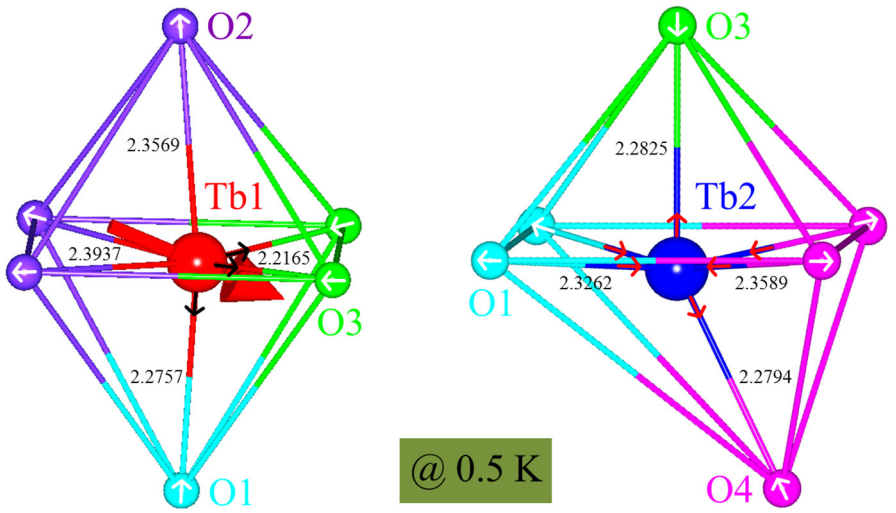

FIGURE 7 | Local octahedral environment of the two Tb sites. The detailed Tb-O bond lengths within the TbO_6 octahedra as refined from the SPODI (FRM-II) data collected at 0.5 K. The big arrow drawn through the Tb1 ion represents the Tb1 moment. The small arrows sitting on the O ions or the Tb-O bonds schematically show the deduced octahedral distortion modes as displayed.

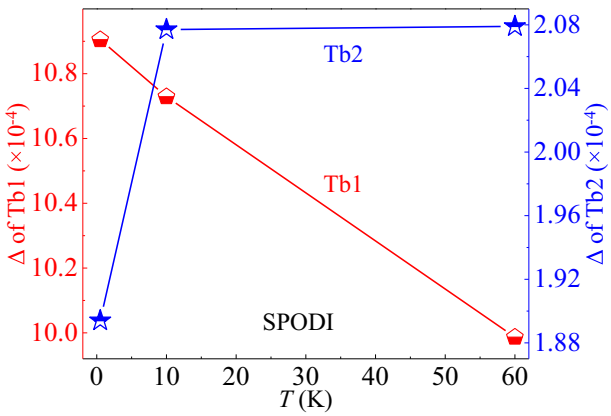

FIGURE 8 | Octahedral distortions of the Tb1 and Tb2 sites. Octahedral distortion parameter Δ of the Tb1 (left ordinate) and Tb2 (right ordinate) sites as refined from the SPODI (FRM-II) data.

attributed to the spatial zigzag-type Tb arrangements along the *a* and *b* axes in the process of forming the crystallographic domains. This is supported by the fact that the honeycomb columns run straightly along the *c* axis, and there is no spin modulation at all in that direction.

Based on the refined Tb-O bond lengths, we deduce two distortion modes for the $Tb1O_6$ and $Tb2O_6$ octahedra (**Figure 7**), respectively. The possible product of the Tb1 subjected stress-vectors (small arrows) should point qualitatively to the direction of the Tb1 moment, implying a strong single-ion anisotropy. This JT-like distortion mode leads to the large Δ value of the Tb1 ions, and possibly lifts further the degenerate multiplets. By contrast, the Tb2 ions are subjected to opposing stresses in all the three pair-directions. In this case, the octahedral distortion strongly depends on their competing strengths. This mode makes the small Δ value of the Tb2 ions and their potential total magnetic moments quenched vitally.

The maximum Tb1 moment size is mere 1.92(6) μ_B, 21.3(7)% of the theoretical saturation value ($g_J J = 9\ \mu_B$). It is of particular interest to explore the frustrating mechanism. The virtual non-Kramers state of the Tb2 site reduces the total moment size per molar formula by 50%. The Tb1 moment fluctuates like a wave defined as $\hat{\mu} = |\hat{\mu}_{max}|cos(Q_{AFM} \cdot R_x + \phi)$, where R_x is a spin coordinate along the *a* axis, and ϕ is a phase parameter. The existence of the strong single-ion anisotropy indicates a large CEF effect which should be comparable to the energy scale of the magnetic interactions. We have shown the clear evidence for a large magnetic exchange anisotropy (**Figure 5**), which is ascribed to the anisotropic dipole-dipole interaction. The NN magnetic arrangement is FM (**Figure 3B**), implying no possibility for a magnetic frustration. The NNN magnetic configurations display a dual character, i.e., FM and AFM for the equivalent Tb11 and Tb12 sites, respectively. This sharp difference may frustrate the Heisenberg-exchange coupled NNN spins.

5. CONCLUSIONS AND OUTLOOK

To summarize, we have synthesized large enough $SrTb_2O_4$ single crystals suitable for neutron scattering and revealed a modulated spin structure in $SrTb_2O_4$ with the highest AFM transition temperature at $T_N = 4.28(2)$ K in the $SrRE_2O_4$ family, which provides a technically friendly platform to explore the related magnetic coupling and frustrating mechanisms. Our studies show that the localized Tb1 moments lie in the *bc* plane with the FM chains along both the *b* and *c* directions and the AFM modulation mainly along the *a* axis. We have found two distinct octahedra for the non-Kramers Tb^{3+} ions: $Tb1O_6$ being strongly distorted, corresponding to the partially-ordered moments; $Tb2O_6$ being frustrated entirely in the non-Kramers state. Therefore,

the octahedral distortion has a decisive influence on the Hund's rule magnetic ground state ($^7F_6$) and the related frustrations. The magnetocrystalline anisotropy is crucial in determining the direction of the ordered moments. The direct NN interaction results in a FM arrangement for the Tb1 ions along the *c* axis, and the different NNN Tb configurations (FM and AFM) further lift the magnetic frustration. The present results make $SrTb_2O_4$ a particularly significant compound in the family for theoretical and further experimental studies. Inelastic neutron-scattering studies to determine the detailed crystal-field and magnetic-interaction parameters would be of great interest. The factors that influence the value of the AFM transition temperature would be further explored in combination with theoretical calculations.

AUTHOR CONTRIBUTIONS

Cong Zhang, Paul Meuffels, and Hai-Feng Li prepared the polycrystals and grew the single crystals. Anatoliy Senyshyn and Hai-Feng Li performed the SPODI experiments and analyzed the data. Martin Boehm, Binyang Hou, and Hai-Feng Li performed the IN3 experiments. Andrew Wildes and Hai-Feng Li performed the D7 experiments and analyzed the data. Karin Schmalzl, Wolfgang Schmidt, and Hai-Feng Li performed the IN12 experiments and analyzed the data. Wolfgang Schmidt, Karin Schmalzl, Eric Ressouche, and Hai-Feng Li performed the D23 experiments. Hai-Feng Li, Cong Zhang, Anatoliy Senyshyn, Andrew Wildes, Karin Schmalzl, Wolfgang Schmidt, Martin Boehm, Eric Ressouche, Binyang Hou, Paul Meuffels, Georg Roth, and Thomas Brückel discussed and analyzed the results. Hai-Feng Li wrote the main manuscript text. Cong Zhang, Anatoliy Senyshyn, Andrew Wildes, Karin Schmalzl, Binyang Hou, Georg Roth, and Thomas Brückel commented on the manuscript and all authors reviewed the paper. Hai-Feng Li conceived and directed the project.

ACKNOWLEDGMENTS

This work at RWTH Aachen University and Jülich Centre for Neutron Science JCNS Outstation at ILL was funded by the BMBF under contract No. 05K10PA3. Hai-Feng Li thanks the sample environment teams at ILL and FRM-II for expert technical assistances.

REFERENCES

1. Santen JHV, Jonker GH. Electrical conductivity of ferromagnetic compounds of manganese with perovskite structure. *Physica* (1950) **16**:599–2. doi: 10.1016/0031-8914(50)90104-2
2. Bednorz JG, Müller KA. Possible high T_c superconductivity in the Ba-La-Cu-O system. *Z Phys B* (1986) **64**:189–5. doi: 10.1007/BF01303701
3. Fiebig M, Lottermoser Th, Fröhlich D, Goltsev AV, Pisarev RV. Observation of coupled magnetic and electric domains. *Nature* (2002) **419**:818–3. doi: 10.1038/nature01077
4. Diep HT. *Frustrated Spin Systems.* Singapore: World Scientific (2004).
5. Lacroix C, Mendels P, Mila F. *Introduction to Frustrated Magnetism. Springer Series in Solid-State Sciences, Vol. 164.* New York, NY: Springer (2011).
6. Li HF, Xiao Y, Schmitz B, Persson J, Schmidt W, Meuffels P, et al. Possible magnetic-polaron-switched positive and negative magnetoresistance in the GdSi single crystals. *Sci Rep.* (2012) **2**:750–6. doi: 10.1038/srep00750
7. Feng YJ, Wang JY, Silevitchb DM, Mihailac B, Kima JW, Yan JQ, et al. Incommensurate antiferromagnetism in a pure spin system via cooperative organization of local and itinerant moments. *Proc Natl Acad Sci USA.* (2013) **110**:3287–92. doi: 10.1073/pnas.1217292110
8. Xiao Y, Su Y, Li HF, Kumar CMN, Mittal R, Persson J, et al. Neutron diffraction investigation of the crystal and magnetic structures in $KCrF_3$ perovskite. *Phys Rev B* (2010) **82**:094437–5. doi: 10.1103/PhysRevB.82.094437
9. Tian W, Li JY, Li HF, Lynn JW, Zarestky JL, Vaknin D. Neutron Scattering Studies of $LiCoPO_4$ & $LiMnPO_4$. *J Phys Conf Ser.* (2010) **251**:012005–5. doi: 10.1088/1742-6596/251/1/012005
10. Li HF. A second-order spin-flop transition in collinear two-sublattice antiferromagnets. (2014) arXiv:1404.3914.
11. Li HF, Hou B, Wildes A, Senyshyn A, Schmalzl K, Schmidt W, et al. The absence of magnetic ordering in the ground state of single-crystal $SrTm_2O_4$: a polarized and unpolarized neutron-scattering study. (2014) arXiv:1404.0044.
12. Morris DJP, Tennant DA, Grigera SA, Klemke B, Castelnovo C, Moessner R, et al. Dirac strings and magnetic monopoles in the spin ice $Dy_2Ti_2O_7$. *Science* (2009) **326**:411–4. doi: 10.1126/science.1178868
13. Gardner JS, Dunsiger SR, Gaulin BD, Gingras MJP, Greedan JE, Kiefl RF, et al. Cooperative Paramagnetism in the Geometrically Frustrated Pyrochlore Antiferromagnet $Tb_2Ti_2O_7$. *Phys Rev Lett.* (1999) **82**:1012–4. doi: 10.1103/PhysRevLett.82.1012
14. Lake B, Tennant DA, Nagler SE. Novel Longitudinal Mode in the Coupled Quantum Chain Compound $KCuF_3$. *Phys Rev Lett.* (2000) **85**:832–4. doi: 10.1103/PhysRevLett.85.832
15. Braun HB, Kulda J, Roessli B, Visser D, Krmäer KW, Güdel HU, et al. Emergence of soliton chirality in a quantum antiferromagnet. *Nat Phys.* (2005) **1**:159–163. doi:10.1038/nphys152
16. Harris MJ, Bramwell ST, McMorrow DF, Zeiske T, Godfrey KW. Geometrical frustration in the ferromagnetic pyrochlore $Ho_2Ti_2O_7$. *Phys Rev Lett.* (1997) **79:**2554–7. doi: 10.1103/PhysRevLett.79.2554
17. Bramwell ST, Gingras MJP. Spin ice state in frustrated magnetic pyrochlore materials. *Science* (2001) **294:**1495–7. doi: 10.1126/science.1064761
18. Lee SH, Broholm C, Ratcliff W, Gasparovic G, Huang Q, Kim TH, et al. Emergent excitations in a geometrically frustrated magnet. *Nature* (2002) **418:**856–8. doi: 10.1038/nature00964
19. Ramirez AP. Geometric frustration: magic moments. *Nature* (2003) **421:**483. doi: 10.1038/421483a
20. Moessner R, Ramirez AP. Geometrical frustration. *Phys Today* (2006) **59:**24–6. doi: 10.1063/1.2186278
21. Han YL, Shokef Y, Alsayed AM, Yunker P, Lubensky TC, Yodh AG. Geometric frustration in buckled colloidal monolayers. *Nature* (2008) **456:**898–903. doi: 10.1038/nature07595
22. Gingras MJP. Observing monopoles in a magnetic analog of ice. *Science* (2009) **326:**375–6. doi: 10.1126/science.1181510
23. Tsymbal EY, Dowben PA. Grand challenges in condensed matter physics: from knowledge to innovation. *Front Phys.* (2013) **1:**32–4. doi: 10.3389/fphy.2013.00032
24. Picozzi S. Ferroelectric Rashba semiconductors as a novel class of multifunctional materials. *Front Phys.* (2014) **2:**10. doi: 10.3389/fphy.2014.00010
25. Morgan JP, Bellew A, Stein A, Langridge S, Marrows CH. Linear field demagnetization of artificial magnetic square ice. *Front Phys.* (2013) **1:**28. doi: 10.3389/fphy.2013.00028
26. Hayes TJ, Balakrishnan G, Deen PP, Manuel P, Chapon LC, Petrenko OA. Coexistence of the long-range and short-range magnetic order components in $SrEr_2O_4$. *Phys Rev B* (2011) **81**:024708–6. doi: 10.1103/PhysRevB.84.174435
27. Fennell A, Pomjakushin VY, Uldry A, Delley B, Prévost B, Désilets-Benoit A, et al. Evidence for $SrHo_2O_4$ and $SrDy_2O_4$ as model J_1-J_2 zigzag chain materials. *Phys Rev B* (2014) **89:**224511–5. doi: 10.1103/PhysRevB.89.224511
28. Kawamura H. Universality of phase transitions of frustrated antiferromagnets. *J Phys Condens Matter* (1998) **10**:4707–48. doi: 10.1088/0953-8984/10/22/004
29. Ramirez AP, Espinosa GP, Cooper AS. Strong frustration and dilution-enhanced order in a quasi-2D spin glass. *Phys Rev Lett.* (1990) **64**:2070–4. doi: 10.1103/PhysRevLett.64.2070
30. Binder K. Ordering of the face-centered-cubic lattice with nearest-neighbor interaction. *Phys Rev Lett.* (1980) **45**:811–4. doi: 10.1103/PhysRevLett.45.811
31. Petrenko OA. Low-temperature magnetism in the honeycomb systems $SrLn_2O_4$ (Review Article). *Low Temp Phys.* (2014) **40:**106–7. doi: 10.1063/1.4865556
32. Barry TL, Roy R. New rare earth-alkaline earth oxide compounds predicted compound formation and new families found. *J Inorg Nucl Chem.* (1967) **29**:1243–6. doi: 10.1016/0022-1902(67)80365-8

33. Pepin JG. Crystal data for $SrRE_2O_4$ (RE = rare earth + Y, In). *J Appl Cryst.* (1981) **14**:70–2. doi: 10.1107/S0021889881008753
34. Karunadasa H, Huang Q, Ueland BG, Lynn JW, Schiffer P, Regan KA, et al. Honeycombs of triangles and magnetic frustration in SrL_2O_4 (L=Gd, Dy, Ho, Er, Tm, and Yb). *Phys Rev B* (2005) **71**:144414–8. doi: 10.1103/PhysRevB.71.144414
35. Balakrishnan G, Hayes TJ, Petrenko OA, M^{c}K DP. High quality single crystals of the SrR_2O_4 family of frustrated magnets. *J Phys Condens Matter* (2009) **21**:012202–3. doi: 10.1088/0953-8984/21/1/012202
36. Ghosh S, Zhou HD, Balicas L, Hill S, Gardner JS, Qiu Y, et al. Short range ordering in the modified honeycomb lattice compound $SrHo_2O_4$. *J Phys Condens Matter* (2011) **23**:164203–5. doi: 10.1088/0953-8984/23/16/164203
37. Wen JJ, Koohpayeh S, McQueen T, Tian W, Li HF, Yan JQ. Magnetic ordering in $SrHo_2O_4$. *APS March Meeting* (2014) **59**:Y4.00008. Available online at: http://meetings.aps.org/link/BAPS.2014.MAR.Y4.8
38. Petrenko OA, Balakrishnan G, Wilson NR, de Brion S, Suard E, Chapon LC. Low-temperature magnetic ordering in $SrEr_2O_4$. *Phys Rev B* (2008) **78**:184410–6. doi: 10.1103/PhysRevB.78.184410
39. Quintero-Castro DL, Lake B, Reehuis M, Niazi A, Ryll H, Islam ATMN, et al. Coexistence of long- and short-range magnetic order in the frustrated magnet $SrYb_2O_4$. *Phys Rev B* (2012) **86**:064203–10. doi: 10.1103/PhysRevB.86.064203
40. Hayes TJ, Young O, Balakrishnan G, Petrenko OA. Magnetisation studies of geometrically frustrated antiferromagnets $SrLn_2O_4$, with Ln = Er, Dy and Ho. *J Phys Soc Jpn.* (2012) **81**:024708–6. doi: 10.1143/JPSJ.81.024708
41. Young O, Wildes AR, Manuel P, Ouladdiaf B, Khalyavin DD, Balakrishnan G, et al. Highly frustrated magnetism in $SrHo_2O_4$: coexistence of two types of short-range order. *Phys Rev B* (2013) **88**:024411–8. doi: 10.1103/PhysRevB.88.024411
42. Cheffings TH, Lees MR, Balakrishnan G, Petrenko OA. Magnetic field-induced ordering in $SrDy_2O_4$. *J Phys Condens Matter* (2013) **25**:256001–6. doi: 10.1088/0953-8984/25/25/256001
43. Li HF. *Synthesis of CMR Manganites and Ordering Phenomena in Complex Transition Metal Oxides.* Jülich: Forschungszentrum Jülich GmbH Press (2008).
44. Hoelzel M, Senyshyn A, Juenke N, Boysen H, Schmahl W, Fuess H. High-resolution neutron powder diffractometer SPODI at research reactor FRM II. *Nucl Instr Methods Phys Res Sec A* (2012) **667**:32–6. doi: 10.1016/j.nima.2011.11.070
45. Ouladdiaf B, Archer J, McIntyre GJ, Hewat AW, Brau D, York, S. OrientExpress: a new system for Laue neutron diffraction. *Physica B* (2006) **385–386**:1052–3. doi: 10.1016/j.physb.2006.05.337
46. Stewart JR, Deen PP, Andersen KH, Schober H, Barthélémy JF, Hillier JM, et al. Disordered materials studied using neutron polarization analysis on the multi-detector spectrometer, D7. *J Appl Cryst.* (2009) **42**:69–84. doi: 10.1107/S0021889808039162
47. Rodríguez-Carvajal J. Recent advances in magnetic structure determination by neutron powder diffraction. *Physica B* (1993) **192**:55–69. doi: 10.1016/0921-4526(93)90108-I
48. Collins MF. *Magnetic Critical Scattering.* London: Oxford University Press (1989).
49. Li HF, Tian W, Yan JQ, Zarestky JL, McCallum RW, Lograsso TA, et al. Phase transitions and iron-ordered moment form factor in LaFeAsO. *Phys Rev B* (2010) **82**:064409–6. doi: 10.1103/PhysRevB.82.064409
50. Li HF, Broholm C, Vaknin D, Fernandes RM, Abernathy DL, Stone MB, et al. Anisotropic and quasipropagating spin excitations in superconducting $Ba(Fe_{0.926}Co_{0.074})_2As_2$. *Phys Rev B* (2010) **82**:140503–5. doi: 10.1103/PhysRevB.82.140503
51. Prokeš K, Hiess A, Bao W, Wheeler E, Landsgesell S, Argyriou DN. Anisotropy of the (π, π) dynamic susceptibility in magnetically ordered (x = 0.05) and superconducting (x = 0.40) $Fe_{1.02}Te_{1-x}Se_x$. *Phys Rev B* (2012) **86**:064503–5. doi: 10.1103/PhysRevB.86.064503
52. Li HF, Yan JQ, Kim JW, McCallum RW, Lograsso TA, Vaknin D. Anisotropic magnetoelastic coupling in single-crystalline CeFeAsO as seen via high-resolution x-ray diffraction. *Phys Rev B* (2011) **84**:220501–5. doi: 10.1103/PhysRevB.84.220501
53. Xiao Y, Nandi S, Su Y, Price S, Li HF, Fu Z, et al. Magnetic anisotropic energy gap and low-energy spin wave excitation in the antiferromagnetic block phase of $K_2Fe_4Se_5$. *Phys Rev B* (2013) **87**:140408–6. doi: 10.1103/PhysRevB.87.140408
54. Zhao J, Adroja DT, Yao DX, Bewley R, Li SL, Wang XF, et al. Spin waves and magnetic exchange interactions in $CaFe_2As_2$. *Nat Phys.* (2009) **5**:555–6. doi: 10.1038/nphys1336
55. Diallo SO, Pratt DK, Fernandes RM, Tian W, Zarestky JL, Lumsden M, et al. Paramagnetic spin correlations in $CaFe_2As_2$ single crystals. *Phys Rev B* (2010) **81**:214407–10. doi: 10.1103/PhysRevB.81.214407
56. Fisher IR, Degiorgi L, Shen ZX. In-plane electronic anisotropy of underdoped '122' Fe-arsenide superconductors revealed by measurements of detwinned single crystals. *Rep Prog Phys.* (2011) **74:**124506–21. doi: 10.1088/0034-4885/74/12/124506
57. Wang C, Zhang R, Wang F, Luo HQ, Regnault LP, Dai PC, et al. Longitudinal Spin excitations and magnetic anisotropy in antiferromagnetically ordered $BaFe_2As_2$. *Phys Rev X* (2013) **3**:041036–6. doi: 10.1103/PhysRevX.3.041036
58. Li HF, Su Y, Persson J, Meuffels P, Walter JM, Skowronek R, et al. Correlation between structural and magnetic properties of $La_{7/8}Sr_{1/8}Mn_{1-y}O_{3+\delta}$ with controlled nonstoichiometry. *J Phys Condens Matter* (2007) **19**:016003–12. doi: 10.1088/0953-8984/19/1/016003
59. Li HF, Su Y, Persson J, Meuffels P, Walter JM, Skowronek R, et al. Neutron-diffraction study of structural transition and magnetic order in orthorhombic and rhombohedral $La_{7/8}Sr_{1/8}Mn_{1-y}O_{3+\delta}$. *J Phys Condens Matter* (2007) **19**:176226–12. doi: 10.1088/0953-8984/19/17/176226
60. Li HF, Su Y, Xiao Y, Persson J, Meuffels P, Brückel Th. Crystal and magnetic structure of single-crystal $La_{1-x}Sr_xMnO_3$ ($x \approx 1/8$). *Eur Phys J B* (2009) **67**:149–9. doi: 10.1140/epjb/e2009-00019-5
61. Ma J, Dela Cruz CD, Hong T, Tian W, Aczel AA, Chi SX, et al. Magnetic phase transition in the low-dimensional compound $BaMn_2Si_2O_7$. *Phys Rev B* (2013) **88**:144405–8. doi: 10.1103/PhysRevB.88.144405

Conflict of Interest Statement: The authors declare that the research was conducted in the absence of any commercial or financial relationships that could be construed as a potential conflict of interest.

Received: 16 May 2014; accepted: 18 June 2014; published online: 21 July 2014.
Citation: Li H-F, Zhang C, Senyshyn A, Wildes A, Schmalzl K, Schmidt W, Boehm M, Ressouche E, Hou B, Meuffels P, Roth G and Brückel T (2014) Incommensurate antiferromagnetic order in the manifoldly-frustrated $SrTb_2O_4$ with transition temperature up to 4.28 K. Front. Phys. 2:42. doi: 10.3389/fphy.2014.00042
This article was submitted to Condensed Matter Physics, a section of the journal Frontiers in Physics.